ENGINEERING TRANSACTIONS • *Engng. Trans.* • **60**, 4, 287–314, 2012
Polish Academy of Sciences • Institute of Fundamental Technological Research (IPPT PAN)
National Engineering School of Metz (ENIM)
SIXTY YEARS OF THE ENGINEERING TRANSACTIONS

Microvoids Evolution in S235JR Steel Subjected to Multi-Axial Stress State

Paweł Grzegorz KOSSAKOWSKI, Wiesław TRĄMPCZYŃSKI

Kielce University of Technology
Faculty of Civil Engineering and Architecture
Chair of Strength of Materials and Concrete Structures
al. Tysiąclecia Państwa Polskiego 7, 25-314 Kielce, Poland
e-mail: {kossak, wtramp}@tu.kielce.pl

The article presents the results of the experimental and numerical analysis of microvoids evolution in elements made of S235JR steel under multi-axial stress state. The numerical simulations were based on the modified Gurson-Tvergaard-Needleman (GTN) material model, taking into account the impact of microstructural defects on the material strength. Two approaches were used, assuming a global and local damage of the structure of S235JR steel. In both cases, the evolution of microdamage (voids) and their impact on the strength and failure of the material were analysed. The results of numerical simulations were similar to the results obtained during microstructural examinations.

Key words: Gurson, Gurson-Tvergaard-Needleman (GTN) material model, multi-axial stress states, S235JR steel, microvoids, numerical simulations.

1. Introduction

The catastrophic failures of engineering structures occuring recently in Poland have led to more extensive research into pre-failure conditions and estimation of limit loads beyond the elastic range. The damage initiation is strongly connected with the different processes, such as overload and corrosion taking place during the operation of the structure. These phenomena reduce the suitability of the structural elements for use, which in an extreme situation may lead to a total destruction of whole structure. In Fig. 1 the corrosion hole is shown as an example of the material structure discontinuity, which strongly reduces the load-bearing capacity of the bridge structural element. Such discontinuity and the thinning of the element's web observed around the corrosion hole changes locally the prevailing strain and stress state, leading to the reduction of the material strength.

FIG. 1. Corrosion hole in bridge structural element.

In the situation analysed, the material is subjected to different (spatial, multi-axial) stress state in comparison to the design assumptions. The transition of the material above the yield strength in a non-linear range may be the most dangerous consequence of discussed damages. It leads to the increase of the stress components which were negligible in the uniaxial stress state. Finally, it may induce the destruction of the individual structural element and ultimately the collapse of the entire structure. Thus, the analysis of multi-axial stress states which may take place during the pre-failure states is especially important issue from a practical point of view and should be subjected to the detailed strength analyses.

For elements under the action of uniaxial stress the strength analysis is relatively easy to conduct. When the failure stress is a three-stress function, the elements are subjected to the multi-axial stress states and the analysis becomes more complicated. In such case, the safety of a steel structure can be assessed using the so called HUBER-MISES-HENCKY (HMH) strength hypotheses, but by assuming the continuum of the material, the HMH model is not suitable to analyse the plastic state of material.

The multi-axial stress state is often realized during experiments with using a tensile bar of circular cross-section with the circumferential annular notch (Fig. 2).

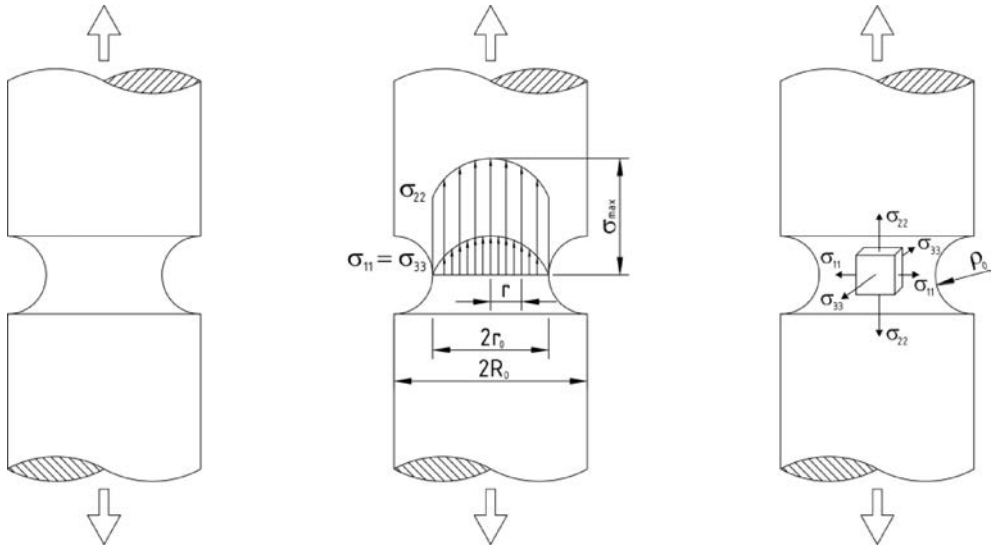

FIG. 2. Geometry and stress state components of a tensile bar of circular cross-section with the circumferential annular notch.

A notch simulates the so-called neck which is observed in the smooth specimens as a result of plasticity in the range of large local deformations. The initial state of stress may be determined by choosing a suitable geometry, in particular, the depth of a notch. Multi-axial state of stress is defined by the so-called stress triaxiality σ_m/σ_e, where σ_m and σ_e denotes the mean normal stress and the effective stress, respectively. For a smooth specimen stress triaxiality reaches limit, minimal value, i.e. $\sigma_m/\sigma_e = 1/3$. For a tensile bar of circular cross-section with a circumferential annular notch the initial stress triaxiality σ_m/σ_e often is determined by using the BRIDGMAN'S solution [1]. For the middle plane of the notch stress triaxiality σ_m/σ_e is defined as

$$\frac{\sigma_m}{\sigma_e} = \frac{1}{3} + \ln\left(\frac{r_0}{2\rho_0} + 1\right), \tag{1.1}$$

where $\sigma_m = (\sigma_{11} + \sigma_{22} + \sigma_{33})/3$ – mean normal stress, σ_e – effective stress, r_0 – initial minimal radius, ρ_0 – initial notch radius.

As can be seen in formula (1.1), when the failure stress is a three-stress function the strength analysis is complicated, especially for damaged elements which are plastically deformed. As mentioned above in such situation, the classical strength hypotheses such as HUBER-MISES-HENCKY (HMH) hypothesis cannot be used due to assuming the continuum of the material structure. The damage material models taking into account the impact of the microdefects of the material structure on the material strength should be applied.

The structural damage of metallic materials, i.e. the process of crack initiation and propagation of polycrystalline structure is closely related to the microstructure of the material. Several basic types of fracture mechanisms such as plastic, cleavage and brittle intergranular, shear or void-sheeting and ductile may be observed [2]. For ductile and shear fracture, the cracking is connected with the nucleation, growth and coalescence of microstructure defects, in the form of voids. Voids are formed on both the material matrix and the existing non-metallic inclusions and second-phase particles. The damage occurs through the growth and coalescence of voids resulting in the development of localised plastic deformations (Fig. 3).

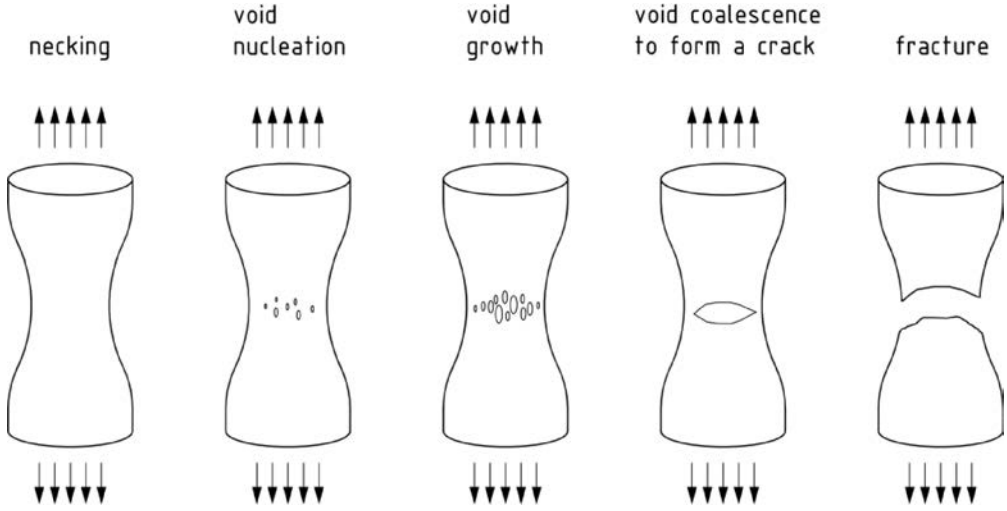

FIG. 3. Ductile fracture micro-mechanism and void evolution in multi-axial stress states.

The evolution of the micro-defects (voids) is one of the significant steps during ductile fracture process. It is a complex phenomenon, depending on many processes such as anisotropy of the voids distribution, spacing, and shape, void nucleation, changes and evolution in void shapes, void-to-void interactions and the nucleation and growth of secondary voids. Voids evolutions determines the localisation of the micro-crack initiation, leading to the process zone forming and finally to the material failure. In many cases, the local damage of the structural elements occurs due to the micro-defects evolution and growth, which in the extreme situation may lead to the total collapse of the structure.

Phenomena described above and connected to ductile fracture of metals can be analysed using damage models taking into account the influence of the microstructural defects on the material strength by defining the relationship between the particular failure stages and the strength of the material, which is shown schematically in Fig. 4.

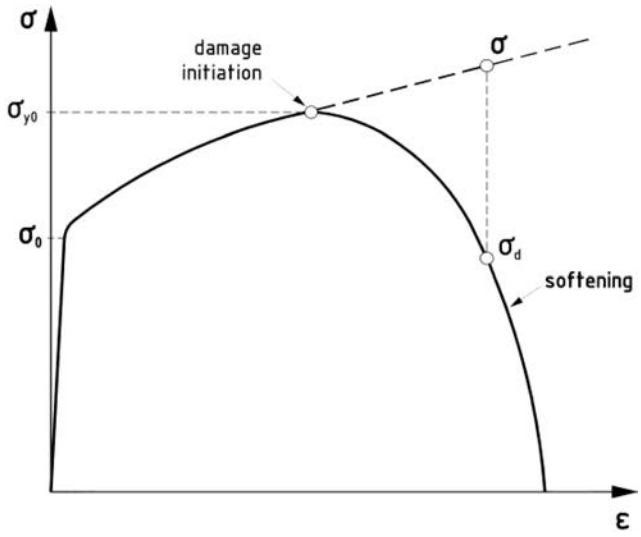

FIG. 4. Reduction of material strength according to general damage material model.

When damage is initiated, the decrease of the material strength is observed, resulting in the decrease of the stress σ_d, determined taking into consideration the damage impact. For the fully dense material, without structural damages, the stress σ increases in whole range of deformation. The decrease of the material strength and stress σ_d is called as softening phenomenon.

One of the first damage material models was GURSON model [3] for porous solids. It was the modification of HMH criterion, defining the influence of an increase in the void volume fraction on the strength of the material, according to the following formula

$$\Phi = \left(\frac{\sigma_e}{\sigma_0}\right)^2 + 2f\cosh\left(\frac{3\sigma_m}{2\sigma_0}\right) - 1 - f^2 = 0, \tag{1.2}$$

where Φ – non-dilatational strain energy, σ_e – effective stress according to the HMH hypothesis, σ_0 – yield stress of the material, σ_m – hydrostatic pressure (mean stress), f – void volume fraction.

The original GURSON failure criterion was further modified by TVEERGAARD [4] and then by TVERGAARD and NEEDLEMAN [5], as a method reffered GTN for the estimation of failure loads resulting from ductile fracture taking into account the microstructural parameters and plastic properties of a material, which is presented in further part of this study.

The GTN method is widely used in various engineering issues. According to the current standards, for instance [6] and its commentary by SEDLACEK *et al.* [7], the GTN model is a basic damage model recommended to use in the analysis of emergency condition for building structures.

Analysing the current state of knowledge on the use of GTN model in the numerical simulation of ductile fracture of steel it can be concluded that there is no comprehensive approach, which allows to carry out numerical calculations for any elements. The numerical simulations are performed using the method of best fit the GTN material parameters for elements with predetermined geometries and strength properties. The GTN parameters are frequently determined basing on the curve fitting technique, without taking into account the typical or boundary parameters values specified in literature. Consequently, the lack of standardised microstructural parameters to develop a GTN model for steels used most commonly in civil engineering is a basic drawback.

Another problem encountered during numerical simulations of nonlinear ranges is proper way of modelling and perform engineering calculations. During simulations of ductile fracture using the finite element method and the GTN model, size effects are encountered, revealing the softening of the final part of the strength curve. Several methods have been tested to minimize the softening effect (e.g. [8–10]), but their applications is limited due to the lack of procedures in the available engineering software.

Taking into consideration the importance of practical issues related to the safety assessment of steel structures and components and described above problems, it is necessary to elaborate a computational procedure which allows the numerical estimation of the limit load capacity of the elements operating in the nonlinear ranges and simulation of the material failure.

Therefore, a wide research program was focused on elaboration of procedures allowing for the numerical analysis of load-bearing capacity of steel building construction elements operating in pre-failure states, taking into account the impact of microdamage using the modified GTN material model. S235JR steel was tested, which is the main steel grade used in construction, so the results will be helpful in analysis and expert opinions on the load-bearing capacity of steel components and structures.

Taking into account that micro-evolution is a fundamental process influencing the state of stress and strain, and directly affects the strength of the material, in the first stage, the research was focused on this issue [11–13] and to develop a methodology of numerical calculations [14]. The next stage of the study includes the determination of GTN model parameters and their sensitivity analysis for S235JR steel.

In contrast to the approach based on matching the material constants for the elements of a particular geometry and strength properties on the basis of curve fitting technique, it is proposed to determine GTN parameters based on actual microstructure and strength parameters determined experimentally. The researches already done were related to the experimental determination of the initial porosity of S235JR steel [11–14].

This article presents the results of experimental and numerical analysis of the evolution of the microstructure damage of S235JR steel. The studies concerned the elements under a multi-axial stress state described by the so-called stress triaxiality σ_m/σ_e, defined as the ratio of mean stress σ_m to effective normal stress σ_e. Taking into account that observed during the studies the effects were most intense for elements with a stress triaxiality above unity [11–13], detailed analysis were performed for elements with the highest value of stress triaxiality, i.e. $\sigma_m/\sigma_e = 1.345$.

In the studies the GTN model parameters such as initial void volume fraction f_0 and TVERGAARD'S parameters q_i were determined experimentally, basing on the actual properties of the microstructure and strength of S235JR steel, as well as the results of studies performed before [11–16].

During the numerical simulations two approaches were used, assuming global and local damage to the material structure. In both cases, the evolution of microdamage (voids) and their impact on the strength and the failure of the material were analysed.

2. MODIFIED GURSON-TVERGAARD-NEEDLEMAN (GTN) DAMAGE MATERIAL MODEL

According to the modified GURSON-TVERGAARD-NEEDLEMAN material model [4, 5] the failure criterion is defined as following

$$\Phi = \left(\frac{\sigma_e}{\sigma_0}\right)^2 + 2q_1 f^* \cosh\left(q_2 \frac{3\sigma_m}{2\sigma_0}\right) - \left(1 + q_3 f^{*2}\right) = 0, \tag{2.1}$$

where Φ – non-dilatational strain energy, σ_e – effective stress according to the HMH hypothesis, σ_0 – yield stress of the material, σ_m – hydrostatic pressure (mean stress), f^* – modified void volume fraction, q_i – TVERGAARD'S parameters describing the plastic properties of the material.

As can be seen, the modified GTN yield criterion (2.1) is described by many material constants, including microstructural properties such as modified void volume fraction f^*, and strength properties defined by TVERGAARD'S parameters q_i and yield stress σ_0.

The modified void volume fraction f^* is defined as follows:

$$f^* = \begin{cases} f & \text{for } f \le f_c, \\ f_c + \dfrac{\overline{f}_F - f_c}{f_F - f_c}(f - f_c) & \text{for } f_c < f < f_F, \\ \overline{f}_F & \text{for } f \ge f_F, \end{cases} \tag{2.2}$$

where f_c – critical void volume fraction at which the void coalescence starts, f_F – void volume fraction corresponding to the complete loss of the material strength, at final separation of the material, $\overline{f}_F = \left(q_1 + \sqrt{q_1^2 - q_3}\right)/q_3$.

As can be seen, at the beginning, when the material is not subjected to the deformation, modified void volume fraction f^* is equal to the initial void volume fraction f_0, being a basic GTN material parameter connected to the material porosity.

TVERGAARD'S parameters q_i have influence on strength properties of the material. The modified void volume fraction f^* is changed by first TVERGAARD'S parameter q_1 in the yield domain (2.1). The strength of the material is decreased for higher values of q_1 parameter, revealing the softening phenomenon due to void growth dominating over hardening properties of the matrix material (Fig. 5a). Higher values of q_1 lead to stronger softening. The optimal value of $q_1 = 1.5$ was proposed by TVERGAARD [4] to model numerically the localisation of plastic deformations effect and fracture phenomena for many porous solids, including metals.

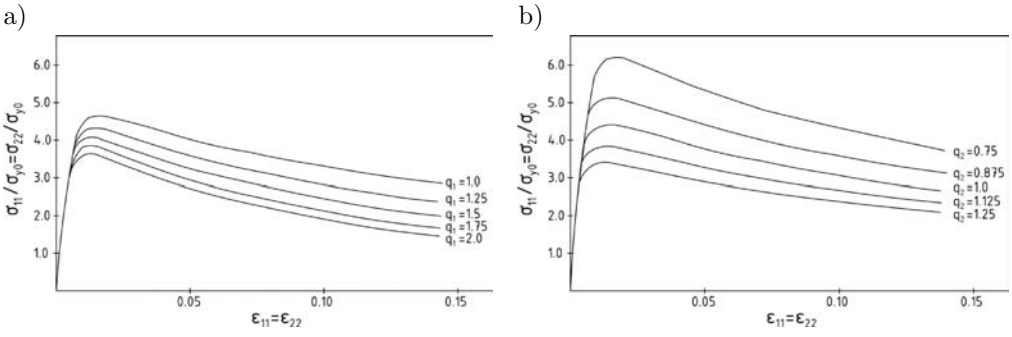

FIG. 5. Influence of TVERGAARD'S parameters q_1 and q_2 on nonlinear response of GTN constitutive law at $\varepsilon_{22}/\varepsilon_{11} = 1.0$ for: a) $1.0 \leq q_1 \leq 2.0$; b) $0.75 \leq q_2 \leq 1.25$ [17].

The second TVERGAARD'S parameter q_2 have impact on the hydro-static component $\sigma_m = \sigma_{kk}/3$, being in relation to the first invariant of the stress state σ_{kk}. The yield limit is strongly reduced for high values of parameter q_2, leading to the strong softening due to the void growth, revealing the annihilation of the strain hardening properties of the matrix material (Fig. 5b). The optimal value $q_2 = 1.0$ was suggested by TVERGAARD [18].

Summing up, typical and suggested values of TVERGAARD'S parameters q_i were established as $q_1 = 1.5$, $q_2 = 1.0$ and $q_3 = q_1^2 = 2.25$ for many metal materials, including steel, being treated as constant for many years. The results of studies of FALESKOG *et al.* [15] revealed, that TVERGAARD'S parameters are dependent on the elastic-plastic properties of the material, such as strain hardening exponent N and yield stress σ_0 to modulus of elasticity E ratio (Fig. 6).

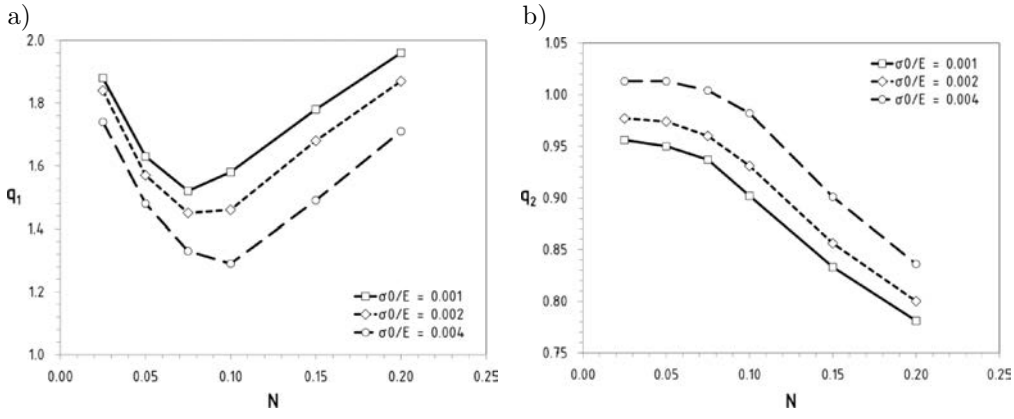

FIG. 6. Correlations q_1 (a) and q_2 (b) to strain hardening N, for different σ_0/E ratios [15].

An increase in the void volume fraction $\dot{f}$ is defined by relationship:

$$\dot{f} = \dot{f}_{\text{gr}} + \dot{f}_{\text{nucl}} = (1-f)\dot{\boldsymbol{\varepsilon}}^{\text{pl}} : \mathbf{I} + \frac{f_N}{s_N\sqrt{2\pi}} \exp\left[-\frac{1}{2}\left(\frac{\varepsilon_{em}^{\text{pl}} - \varepsilon_N}{s_N}\right)^2\right] \cdot \dot{\varepsilon}_{em}^{\text{pl}}, \tag{2.3}$$

where: $\dot{f}_{\text{gr}}$ – change due to growth of voids existing in the material, $\dot{f}_{\text{nucl}}$ – change due to nucleation of new voids, f_N – volume fraction of nucleated voids, s_N – standard deviation of nucleation strain, $\dot{\boldsymbol{\varepsilon}}^{\text{pl}}$ – plastic strain rate tensor, $\mathbf{I}$ – second-order unit tensor, ε_N – mean strain of the void nucleation, $\varepsilon_{em}^{\text{pl}}$ – equivalent plastic strain in the matrix material, $\dot{\varepsilon}_{em}^{\text{pl}}$ – equivalent plastic strain rate in the matrix material.

3. GTN model parameters of S235JR steel

3.1. Microstructural examinations

The first step of the material examinations was to obtain the images of the microstructure of S235JR steel [19]. The images were taken using the light metallographic microscope with magnification $\times 100 \div 1000$. The sections were cut of the material intended to the strength tests. After the sections were cut out, the specimens were digested and polished.

S235JR steel belongs to a group of low, mild carbon steel having a maximum carbon content of C = 0.2% and the maximum contents of elements: Mn = 1.40%, P = 0.035%, S = 0.035% and N = 0.012%.

The observed microstructure was a ferritic-perlitic type (Fig. 7a). In longitudinal section the ferrite grain were equally axial, while pearlite grains were elongated by the material forming (rolling). The contribution of perlite was es-

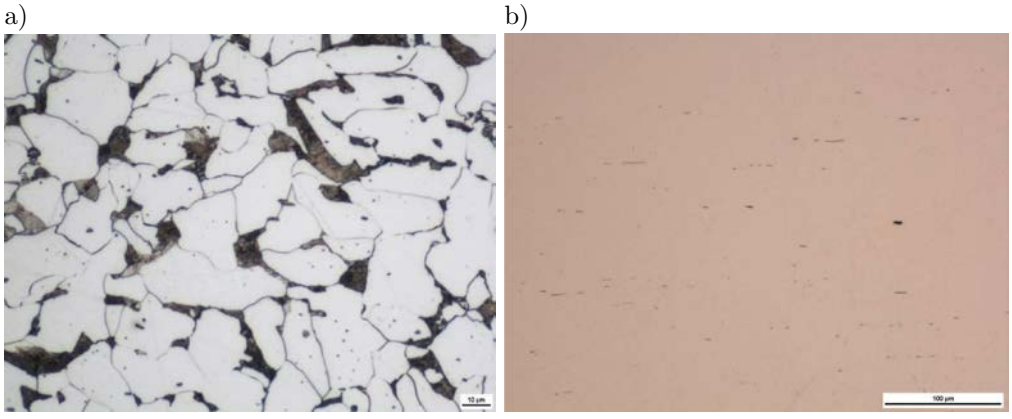

FIG. 7. Microstructure of S235JR steel: a) sample after digestion, b) sample after polishing [19].

timated to be approximately 10–20%. As can be seen in Fig. 7b, there are a large number of non-metallic inclusions.

Observed non-metallic inclusions are mainly sulfides and brittle oxides. The sulphide inclusions were characterized by an elongated shape and their length reached up to 61.9 μm. These inclusions were irregularly distributed in the volume of material and formed the bands. The second type of non-metallic inclusions were brittle oxide inclusions. They have a shape close to rectangular and sometimes occurred with sulphide inclusions.

In order to fully characterize the tested material in terms of the observed non-metallic inclusions, the basic parameters of the stereological for inclusions were measured. The initial void volume fraction of the inclusions was estimated at a maximum level of 0.17% (for the central part of the cross section).

3.2. Strength tests and numerical simulations

In order to determine the strength parameters of S235JR steel the standard static tensile test was performed for specimens with a circular cross-section, according to [20]. The tests were performed using 322 MTS testing machine with capacity of 100 kN and a hydraulic drive with controlled increase of displacement (Fig. 8b).

The nominal diameter of the specimens was $d = 10$ mm, the length of the measuring base $l_0 = 50$ mm, and the primary cross-sectional area $S_0 = 78.5$ mm^2 (Fig. 8a). The number of the test was $n = 8$ specimens.

The average values of strength parameters for the significance level of 0.05 were obtained as follows: the yield stress $R_{0.2} = 318.3 \pm 2.59$ MPa with standard deviation $s = 3.73$ MPa, the tensile strength $R_m = 457.4 \pm 4.91$ MPa with

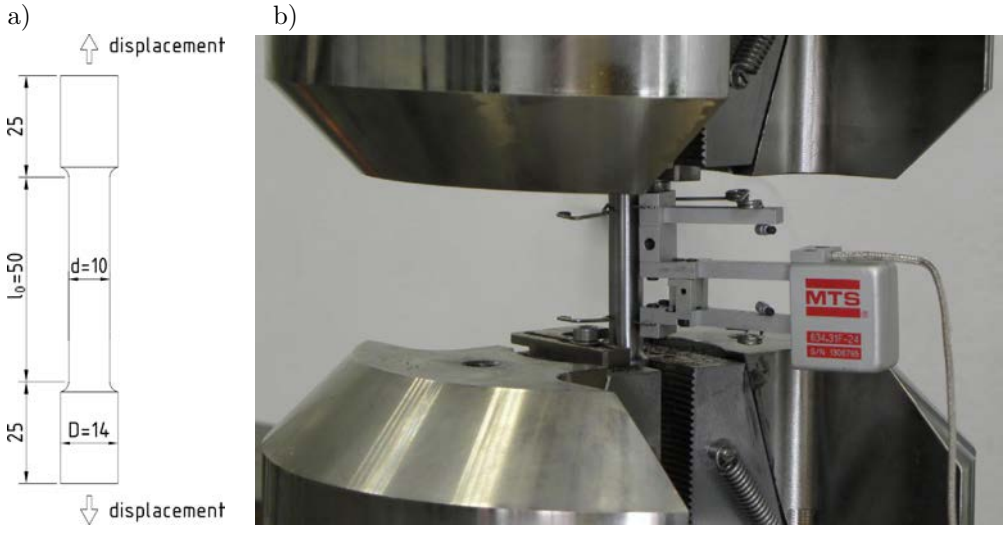

FIG. 8. Sample used in strength tensile tests of S235JR steel (a); sample subjected to tension (b).

standard deviation $s = 7.09$ MPa, and the percentage elongation $A_t = 33.3 \pm 1.47\%$ with standard deviation $s = 2.13\%$. The modulus of elasticity was $E = 205$ GPa and coefficient of transverse elasticity was $G = 80$ GPa. During the test the nominal normal stress σ and the longitudinal strain ε were determined as a function $\sigma(\varepsilon)$.

3.3. Determination of material parameters of GTN model

Material parameters of GTN model for S235JR steel were determined basing on the results of microstructural studies, strength parameters and numerical modeling of the standard tensile test and results obtained in previous studies [11–14].

The initial void volume fraction was determined during the microstructural examinations shown in Subsec. 3.1 as $f_0 = 0.0017 = 0.17\%$ [19].

The TVERGAARD'S parameters were determined according to results obtained by FALESKOG *et al.* [15] and established as $q_1 = 1.90$, $q_2 = 0.81$ and $q_3 = 3.61$ for the ratio $R_{0.2}/E = 0.00155$ with strain-hardening exponent $N = 0.183$.

Other parameters of the model for S235JR steel were assumed to fit final results (Fig. 19) and according to data obtained during tests carried out by the authors [11–14].

Numerical calculations were performed using a program based on finite element method Abaqus Explicit 6.10. The elements were modelled as an axially-symmetric, using standard CAX4R elements [21]. The model parameters were

determined based on the tensile curves $\sigma(\varepsilon)$ determined experimentally and fitted by numerical simulations. At each iteration step, the values of the GTN model parameters were changed within certain limits. The optimization criterion was the convergence of the $\sigma(\varepsilon)$ values obtained numerically and experimentally.

During the numerical simulation elastic-plastic properties of S235JR steel were described by appromaximating function as following:

$$\frac{\sigma}{\sigma_0} = \left(\frac{\sigma}{\sigma_0} + \frac{3G}{\sigma_0}\varepsilon^{\mathrm{pl}}_{e\,m}\right)^N, \tag{3.1}$$

where σ – stress, σ_0 – yield stress of the material, $\varepsilon^{\mathrm{pl}}_{e\,m}$ – equivalent plastic strain in the matrix material, G – coefficient of transverse elasticity, N – strain-hardening exponent.

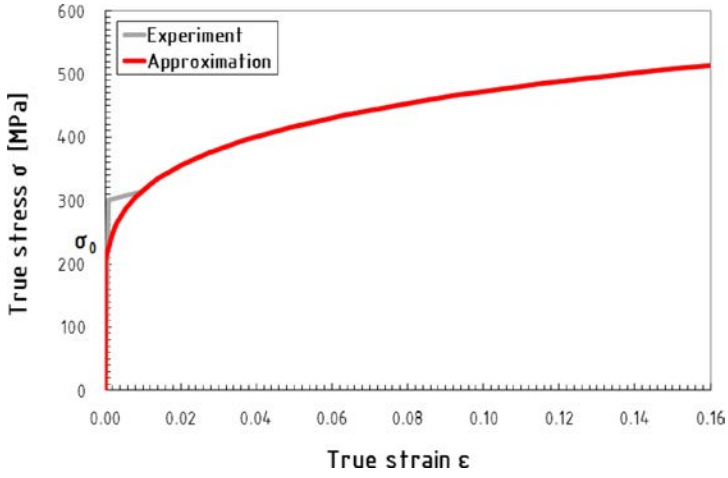

FIG. 9. Approximation of tensile curve $\sigma(\varepsilon)$ according to Eq. (3.1).

At the end:

- the critical value of volume fraction f_c, above which the nominal material strength decreased, was assumed as $f_c = 0.06$ (as suggested by RICHELSEN and TVERGAARD [22], the critical value of the void volume fraction, f_c, is dependent on the initial void volume fraction f_0). It ranges from $f_c = 0.04$ at $f_0 = 0.0$ to $f_c = 0.12$ at $f_0 = 0.06$,
- the value of the void volume fraction corresponding to the complete loss of material strength f_F was assumed as $f_F = 0.667$ in order to analyse whole range of material deformations, especially at the failure range,
- other GTN material parameters were assumed as following: the volume fraction of the nucleated voids $f_N = 0.04$, the average nucleation (initiation) strain of inclusion-related voids $\varepsilon_N = 0.3$, and the standard deviation of the nucleation strain $s_N = 0.05$.

All parameters of GTN model for S235JR steel are summarized in Table 1, the parameters determined experimentally are marked with bold.

Table 1. Microstructural parameters of GTN model of S235JR steel.

f_0	f_c	f_F	q_1	q_2	q_3	ε_N	f_N	s_N
0.0017	0.06	0.667	**1.90**	**0.81**	**3.61**	0.30	0.04	0.05

4. Analysis of microvoids evolution in S235JR steel

4.1. Strength tests of tensile elements under multi-axial stress state

As part of a wide research program [11–14] the tensile specimens with circular cross-sections for different notch radii ρ_0 (Fig. 10) were tested. It allowed to obtain the multi-axial stress state defined by stress triaxiality ranged from $\sigma_m/\sigma_e = 0.556$ up to $\sigma_m/\sigma_e = 1.345$, according to Bridgman's solution Eq. (1.1).

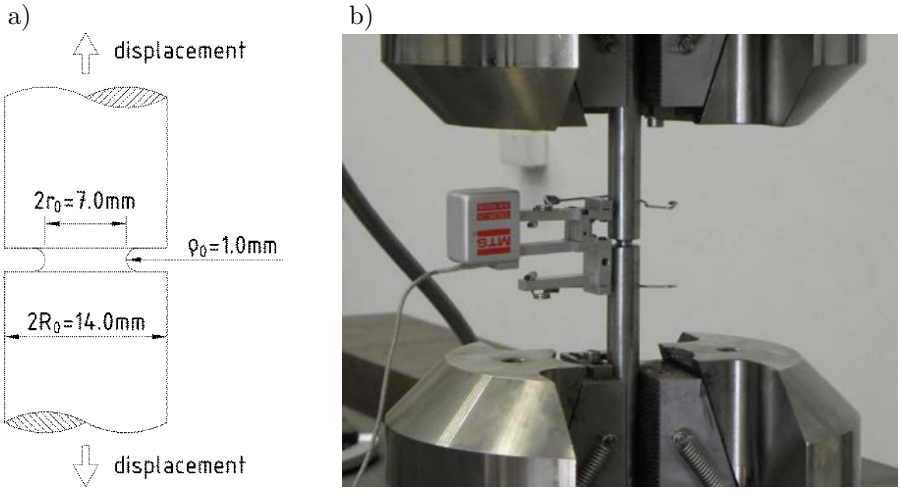

Fig. 10. Geometry (a) and view of ring-notched round specimen subjected to tension in multi-axial stress state (b).

Taking into account that observed during the studies [11–14] the effects were most intense for elements with a high stress triaxiality, for $\sigma_m/\sigma_e > 1$, detailed analysis was performed for elements with the highest value of stress triaxiality, i.e. $\sigma_m/\sigma_e = 1.345$.

The elements with diameters of $2R_0 = 14.0$ mm and $2r_0 = 7.0$ mm and the bottom of the notch radius $\rho_0 = 1.0$ mm were tested, which allowed to obtain a multi-axial state of stress corresponding to the value of stress triaxiality $\sigma_m/\sigma_e = 1.345$. The experimental examinations included tensile strength tests, during

which specimens were subjected to static tension. The quantities measured were force F and displacement of points distributed symmetrically along the specimen l, with the extensometer initial length being $l_{0s} = 32.56$ mm (Fig. 10).

4.2. Microstructural examinations of microvoids evolution

In this part of the research the microstructural images of fracture areas (Fig. 11) and microsections (Fig. 13) of samples subjected to strength tests were made. The sections were cut of the notched tensile specimens subjected to multi-axial stress state according to a scheme shown in Fig. 12. After the sections were cut out, the samples were digested.

a) b)

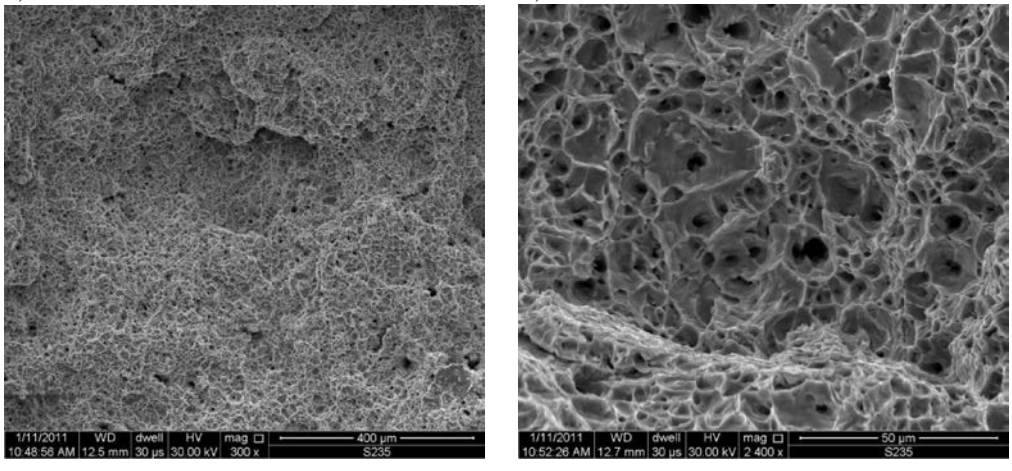

FIG. 11. The microstructure of fracture: a) magnification ×300, b) magnification ×2400.

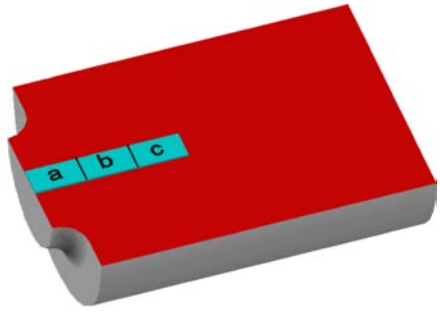

FIG. 12. Denotation of particular microsections (a), (b) and (c).

The scanning photography technique was applied, with using the scanning microscope JEOL JSM-5400 with maximum magnification of 200 000.

The numerous voids around the non-metallic inclusions (Fig. 11) were observed in the fracture area. The voids were formed by the separation of foreign

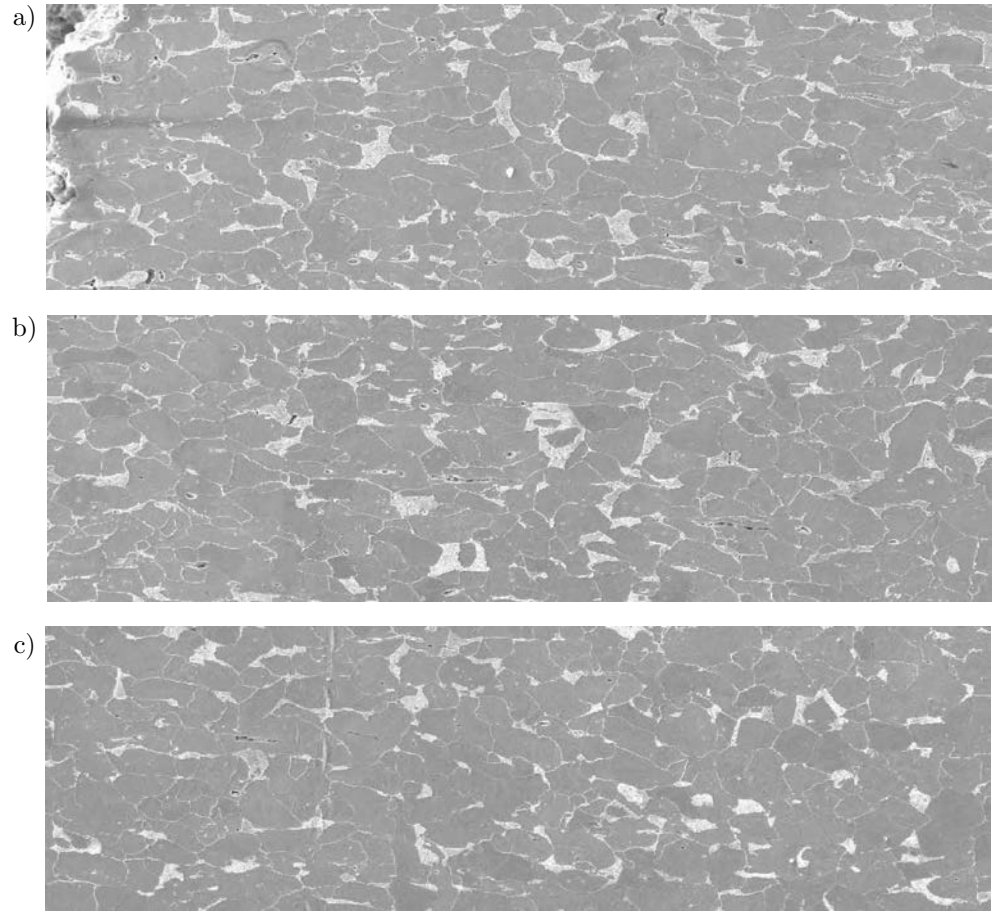

FIG. 13. The images of particular microsections (a), (b) and (c) according to Fig. 12.

phase particles (inclusions) from the matrix. The consequence of the process was the nucleation of voids at the inclusions and the growth and interconnection of the voids during further deformation. The intensity of the process of void nucleation and growth decreased as the distance from the fracture area increased. This was mainly due to changes in the stress state and a smaller deformation of the specimen.

In the region below the fracture area around the notch (Fig. 13c) some nonmetallic inclusions were noticed also. They were underwent a slight deformation in comparison to the region of fracture area, consequently the process of void nucleation and growth did not occur in this region.

The phenomenon of void nucleation and growth was observed only in the area of strong plastic deformation, i.e. in the fracture area, which was confirmed by a numerical analysis discussed further in the paper.

4.3. Numerical simulation of microvoids evolution

In the next stage of the analysis the numerical calculations were carried out, in order to simulate the evolution of microvoids during the plasticity process of S235JR steel until the complete failure of the material.

The numerical calculations were performed using Abaqus version 6.10. The samples of circular cross section with a ring notch of radius $\rho_0 = 1.0$ mm used during the strength tests described previously, were modelled. The specimens were subjected to static tension at a controlled rate of displacement 4 mm/min, similarly as in the experiments. Samples were modelled as an axially symmetric, using the standard elements of the 4-nodal CAX4R [21]. Due to the symmetry of the problem, only quarter of the samples were modelled. The height of numerical models corresponded to half the length of the extensometer, i.e. 16.28 mm.

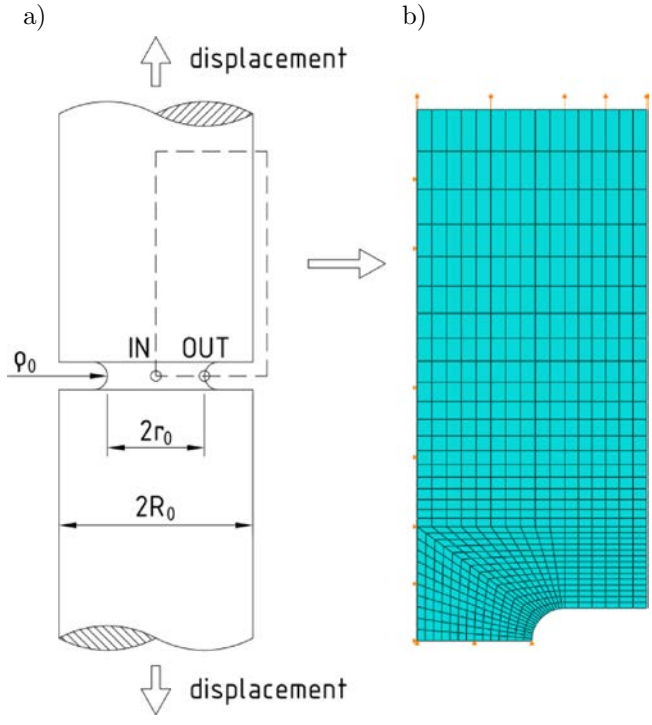

FIG. 14. Tested element (a); numerical model (b).

The modified Gurson-Tvergaard-Needleman (GTN) material model was used with a nonlinear dynamic analysis explicite.

During numerical simulations two approaches were applied:

- *GTN model*, a global approach,
- *Cell model*, a local approach.

4.3.1. GTN Numerical Model. The global approach was used assuming a model of a porous GTN material model for whole numerical model, as shown in Fig. 15. The GTN material parameters were assumed according to the values given in Subsec. 3.2 (Table 1). The results obtained using this approach are marked on charts as *GTN model*.

The mesh in the region close to the fracture plane, so-called *process zone*, was modelled with using finite elements of width equal to 250 μm, while the height of the finite elements was different, ranging from 50 μm up to 350 μm, as it is shown in Fig. 15.

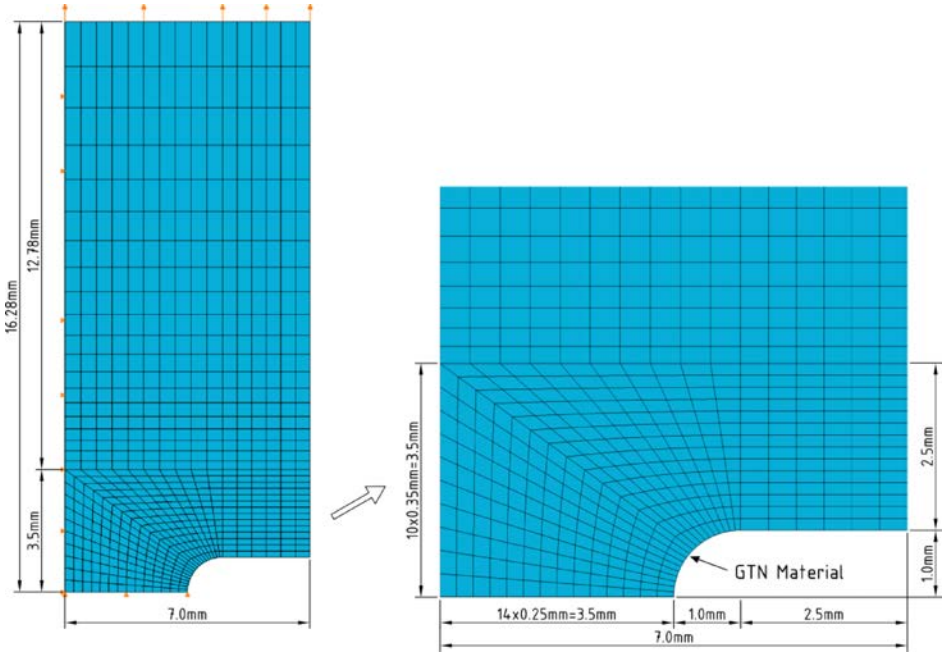

FIG. 15. *GTN* numerical model.

4.3.2. Cell Numerical Model. The second approach was based on observations of the formation and evolution of the microstructure of S235JR steel and the results of the analysis contained in [11–16, 23, 24]. As mentioned before, the failure of many metals is due to increased microdamage. This mechanism reveals the macroscopic, local, the so-called *process zone* of a thickness corresponding to one-, two distances between microdamages and it is characterised by considerable plastic deformations. Outside of this area, voids does not show significant growth, which reveals their minimal impact on the softening of the material and decrease its strength.

Numerical implementation of the above phenomena in numerical computation is based on the separation of the area directly adjacent to the crack plane

and using the material model takes into account the microdamage there, such as GTN model. For the rest of numerical model the elastic-plastic material with no damage of the microstructure is used (Fig. 16). The model of porous material is assumed locally to the area in which a significant increase of microvoids and the initiation of cracking is expected.

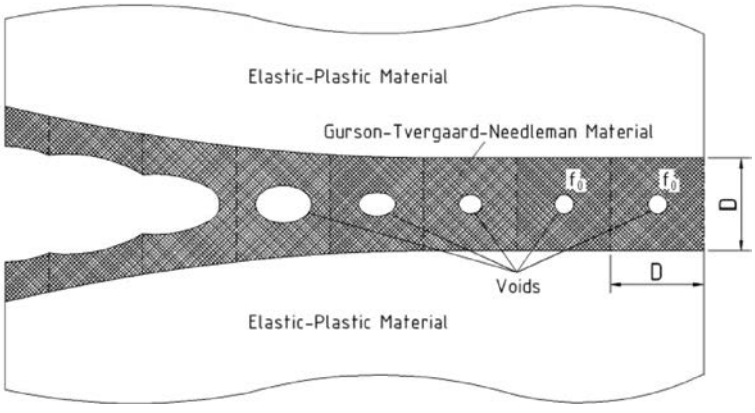

FIG. 16. Implementation of *Cell* method in numerical calculations (basing on Ref. [15]).

The basic issue is the assuming of an appropriate size of the *process zone*, so that the softening of the material to represent the physical processes occurring. Taking into account the results of analysis carried out for tensile elements [14], the thickness of the *process zone* was assumed based on the method proposed by HANCOCK and MACKENZIE [25]. The size of *process zone* defines the characteristic length l_c in the field of high stress and deformations. According to the assumptions of this method, the failure of the material occurs as a result of linking one or two cavities formed from colonies formed by the coalescence of micro-inclusions initiated on second-phase particles. Length l_c is identified with the size of the cavities and micro-colony and it is determined by analysis of the microstructure fractures.

Basing on the results of studies performed before [14] the size of the *process zone* was defined as the average dimensions of an inclusion colony, i.e. characteristic length l_c, and determined during the microstructural examinations. The size of inclusion colony was identified as the average dimensions of the measured plateaus and valleys on the castellated fracture surface. During the measurements the CHAUVENET'S criterion was applied and all a typical values were rejected. Twenty measurements were made. The size of *process zone* ranged from 140 to 370 mm, and the average value was determined as $D \approx 250$ μm (Fig. 17).

The porous GTN material was assumed in numerical model for the layer adjacent to the plane of fracture (Fig. 18). Considering the symmetry of the problem, the thickness of the layer modelling *process zone* was assumed as 125 μm.

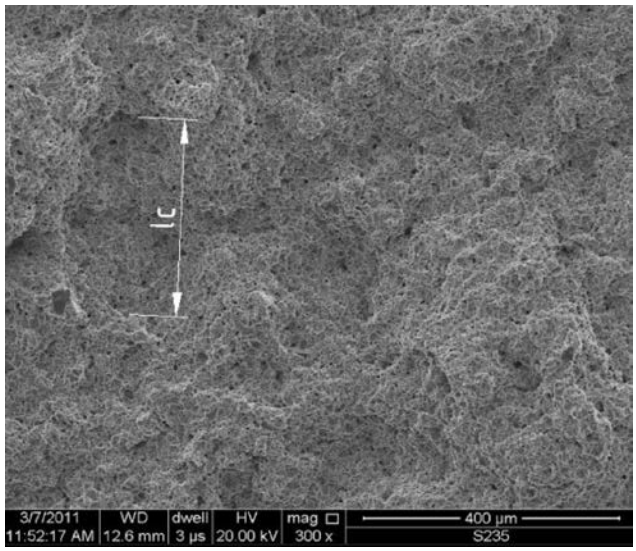

FIG. 17. Determination of dimensions of process zone identified as characteristic length l_c.

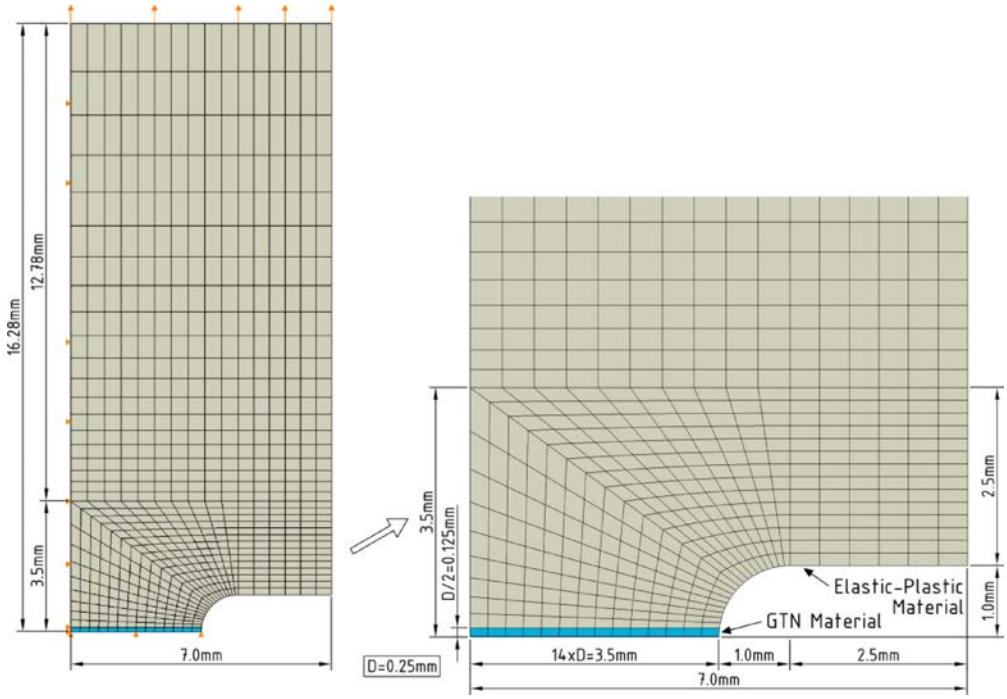

FIG. 18. *Cell* numerical model.

For the rest of the numerical model the elastic-plastic material was assumed basing on the approximating function (3.1). The results obtained using this approach are referred as *Cell model*.

4.3.3. Result of numerical analysis. Numerical simulation of microvoids evolution was based on an analysis of changes in the Void Volume Fraction (VVF) following in the plasticity process of S235JR steel. Based on the results of experimental studies and numerical simulations using *GTN* and *Cell models*, force-elongation curves $F(l)$ for the corresponding points based on extensometer were obtained. The Void Volume Fraction VVF curves as a function of elongation l for the center of elements at the point marked as IN and the bottom of the notch at the point labelled OUT (according to Fig. 14) were obtained.

As is clear from the force-elongation curves $F(l)$ for all analyzed elements the force F determined in numerical simulations are consistent with the results of experimental studies. For both used models, *GTN* and *Cell*, for the range from maximal force F up to the material failure the compatibility of the results obtained numerically and experimentally was noticed (Fig. 19).

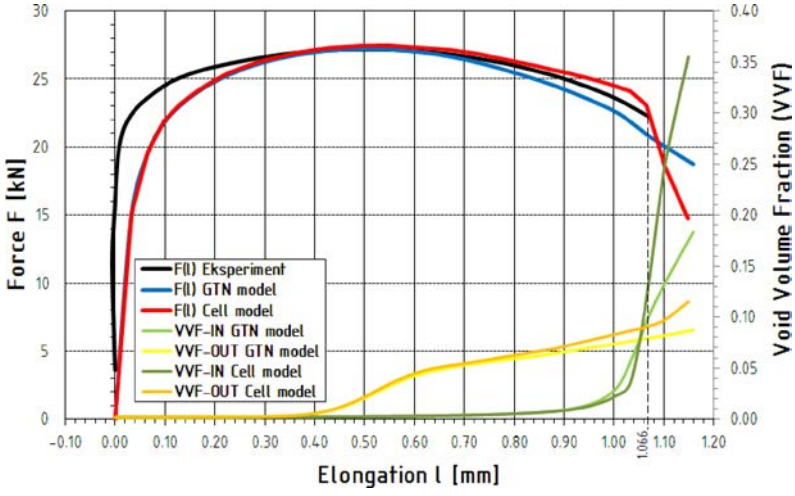

FIG. 19. Force F and Void Volume Fraction VVF *versus* elongation l curves for points IN and OUT.

Differences in the values of $F(l)$ reveals the end of their parts, when the maximum force is exceeded.

When using the *GTN model*, a slight *softening* phenomenon was observed, progressing in ever greater extent up to the failure. In the final phase of deformation, the noticeable changes in the slope of the curve $F(l)$ is noticed, but no sudden decrease of force is observed at the failure moment, which corresponds to the elongation reached a value of $l = 1.066$ mm. When *Cell model* was used, the opposite effect was observed, i.e. higher values of force F compared to the value determined during the experiments. At the moment of failure the curve $F(l)$ determined numerically falls rapidly, until the total loss of the load-bearing capacity of the element.

Analysing the process of microvoids evolution it should first be noted that in all the analysed elements in the initial stages of deformation, there was no nucleation and growth of voids (Fig. 19). The beginning of the process of nucleation and growth of the void volume fraction was observed just before the maximum force was achieved. The initial process of growth of voids was particularly intense in the outer parts, for the point labelled OUT. After the maximum force was achieved, the rate of growth of voids increases, which corresponds to the elongation $l \approx 0.90$ mm. At the moment just before the failure, for $l = 1.05$ mm, the beginning of the rapid growth of voids in the middle of the sample (in point IN) compared with the external part (in point OUT) was observed. In the further process of deformation the voids increased much more intensively and faster in the middle part of elements in relation to the outside part (Fig. 21–23, and 26–28). It can be concluded that in all analysed cases, the failure proceeded from inside to outside elements.

For both, the *GTN* and *Cell model*, the mechanism of nucleation and microvoids evolutions is similar (Fig. 20, 25). In the outer parts of the elements, the void nucleation occurs at the the level of elongation $l \approx 0.40$ mm, and quickly stabilizes at $l \approx 0.65$ mm. A further evolution of voids is due to their growth. In the case of the inner part of the elements the process described above is similar, but occurs much later, for elongations $l \approx 0.95$ mm and $l \approx 1.05$ mm respectively. Similarly to the differences in the final force-elongation curves obtained using the *GTN* and *Cell models*, the differences in curves of Void Volume Fraction *VVF* were observed in the final phase of simulation, for $l > 1.05$ mm, for the phase corresponding to the material failure. The higher growth rate of *VVF*

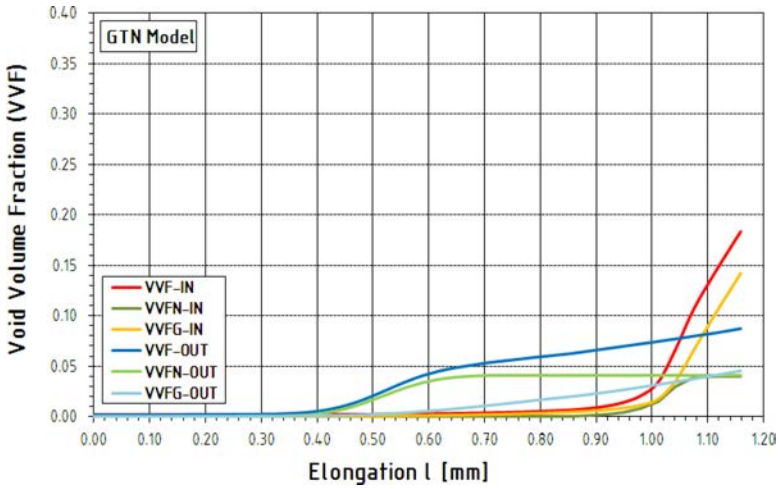

FIG. 20. Void Volume Fraction *VVF*, Void Volume Fraction due to Void Nucleation *VVFN* and Void Volume Fraction due to Void Growth *VVFG versus* elongation l curves for points IN and OUT, *GTN model*.

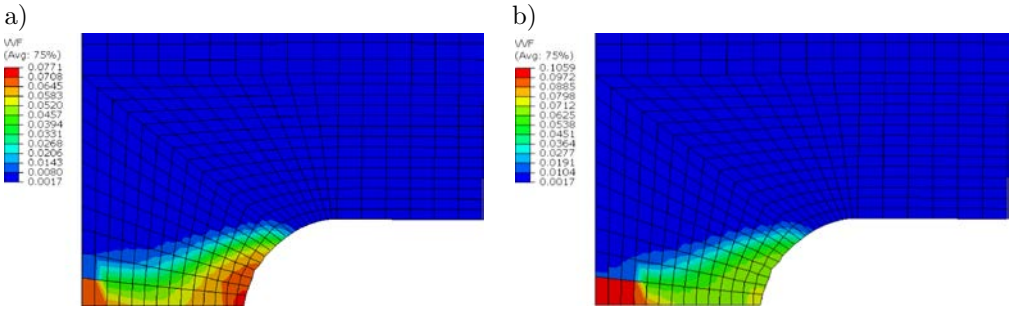

FIG. 21. Void Volume Fraction *VVF* maps, *GTN model*: a) $l = 1.04$ mm, b) $l = 1.07$ mm.

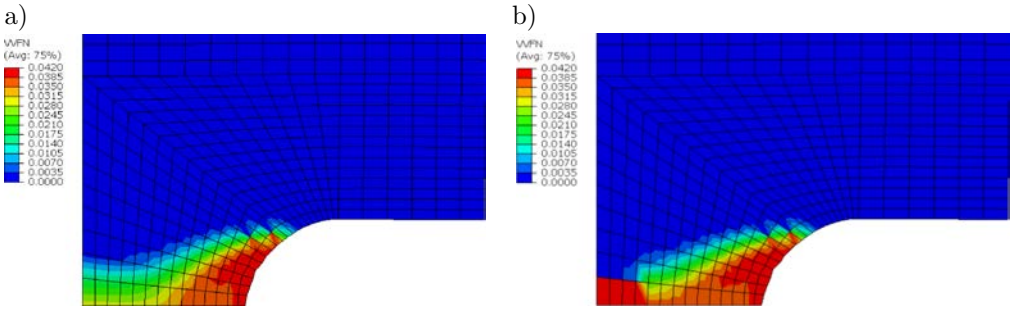

FIG. 22. Void Volume Fraction due to Void Nucleation *VVFN*, *GTN model*: a) $l = 1.04$ mm, b) $l = 1.07$ mm.

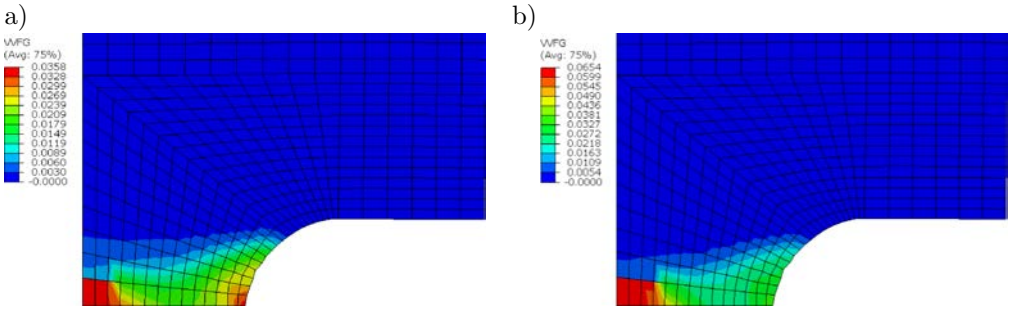

FIG. 23. Void Volume Fraction due to Void Growth *VVFG, GTN model*: a) $l = 1.04$ mm, b) $l = 1.07$ mm.

was observed using the *Cell model* in comparison to the *GTN model*. Critical values of Void Volume Fraction $VVF = 0.10$ and $VVF = 0.13$ at the material failure were noticed for $l = 1.066$ mm, respectively for the *GTN* and *Cell model* (Fig. 19, 20 and 25). In a further range of simulation increasingly higher values of *VVF* were observed when using *Cell mode*l compared to *GTN model*.

It can be seen clearly that the use of local softening of the material by using the *Cell model* has significant effects on the evolution of microdamage as

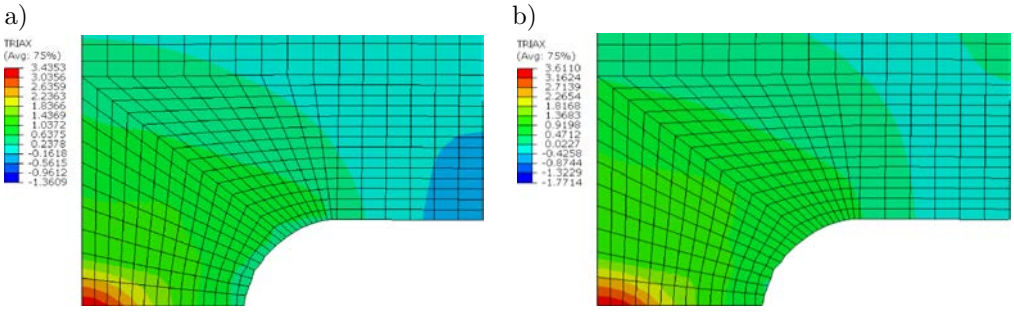

FIG. 24. Stress triaxiality maps σ_m/σ_e, *GTN model*: a) $l = 1.04$ mm, b) $l = 1.07$ mm.

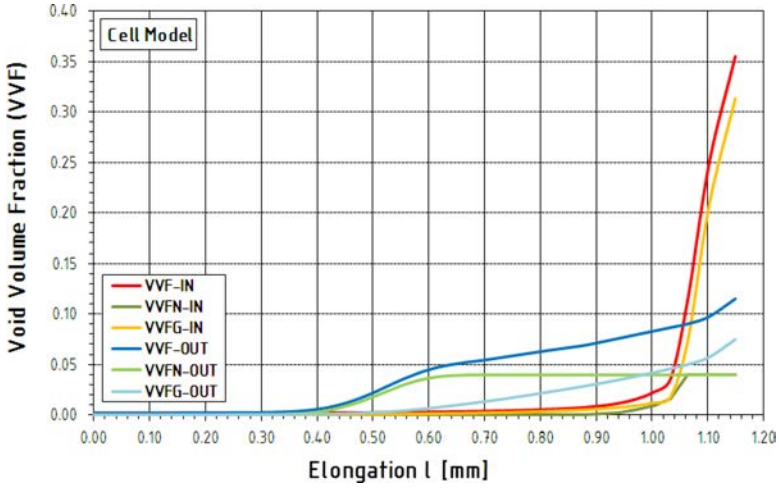

FIG. 25. Void Volume Fraction *VVF*, Void Volume Fraction due to Void Nucleation *VVFN* and Void Volume Fraction due to Void Growth *VVFG versus* elongation l curves for points IN and OUT, *Cell model*.

compared to the global approach, the *GTN model*. Assuming the porous material only in parts of an element leads on the one hand to the global strengthening, on the other hand, when the microvoids are growing, indicates a sudden drop in force, rapidly leading to the failure of the material.

Observed phenomena of evolution of microdamage described above are closely connected to changes in stress state around the bottom of the notch. When the load decreased, corresponding to the beginning of the material failure process, the increase of stress σ_m/σ_e was observed. These changes were less noticeable when using *GTN model*, where at the material failure the maximum value of σ_m/σ_e increased from of the value of $\sigma_m/\sigma_e = 3.44$ to $\sigma_m/\sigma_e = 3.61$ at the middle of element (Fig. 24). In the case of *Cell model* the above phenomena were more intense, because σ_m/σ_e increased almost twice, from $\sigma_m/\sigma_e = 2.12$ up to $\sigma_m/\sigma_e = 4.16$ (Fig. 29).

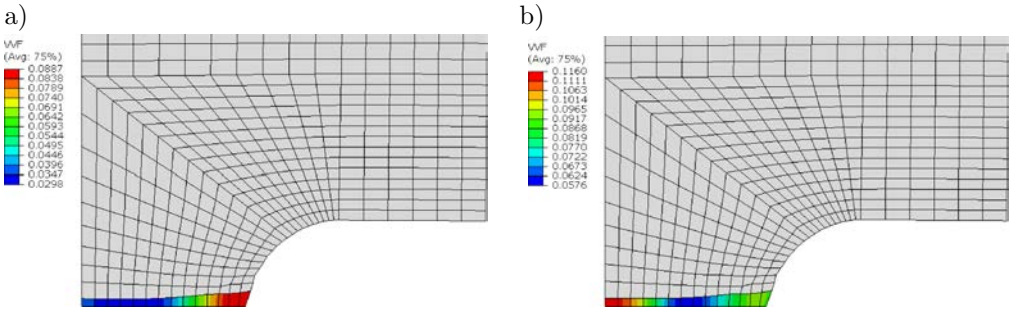

FIG. 26. Void Volume Fraction *VVF* maps, *Cell model*: a) $l = 1.06$ mm, b) $l = 1.10$ mm.

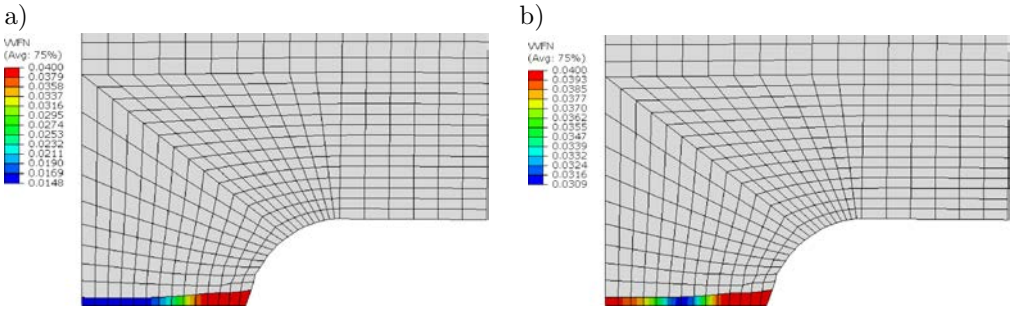

FIG. 27. Void Volume Fraction due to Void Nucleation *VVFN*, *Cell model*: a) $l = 1.06$ mm, b) $l = 1.10$ mm.

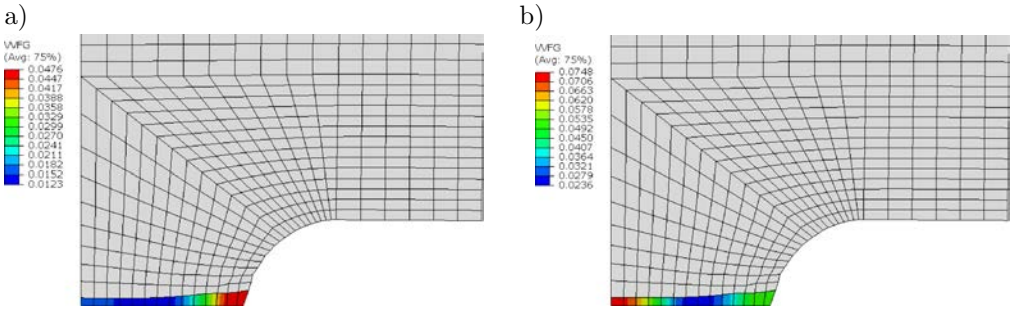

FIG. 28. Void Volume Fraction due to Void Growth *VVFG*, *Cell model*: a) $l = 1.06$ mm, b) $l = 1.10$ mm.

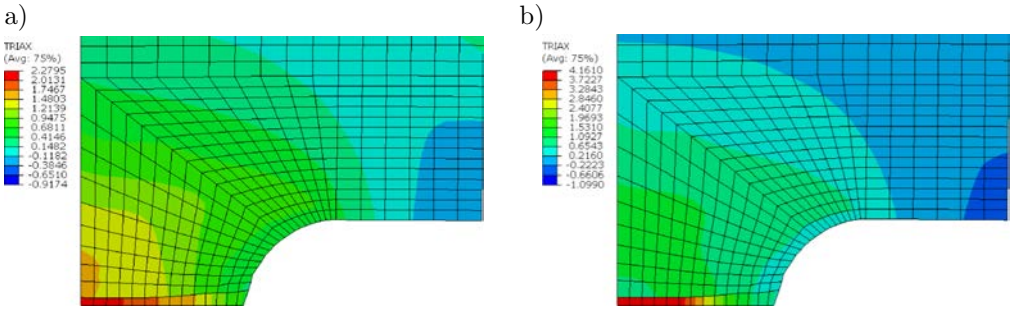

FIG. 29. Stress triaxiality maps σ_m/σ_e, *Cell model*: a) $l = 1.06$ mm, b) $l = 1.10$ mm.

Another characteristic phenomenon observed in all analysed elements was that the damage growth followed in a very small volume of material. Growth of voids included elements lying directly in the plane of the smallest cross section, near the bottom of the notch (Fig. 21–23). The same conclusion are drown from both the microstructural studies and numerical simulations.

From the point of view of micro-simulation of the evolution of the material structure, using in numerical calculations the local approach gives qualitatively better results in comparison with the classical global approach. The assuming of the so-called *process zone*, however, requires determining in advance the places where one would expect nucleation and growth of microvoids, leading eventually to the failure. In very complicated cases, where it is difficult to one hundred percent certainty correctly identify the location and extent of *process zone*, the local approach could lead to errors, resulting in an underestimation or overestimation of the carrying capacity of the element. In such a situation it should be a two-step calculations applied, pre-specifying the damaged area, by using for example global *GTN model*. In the next stage of the calculation, with already defined *process zone*, it would be possible to assume a local approach, e.g. using *Cell* method.

5. Conclusions

The article presents the results of analysis of the microdamage evolution of S235JR steel under multi-axial stress state, based on the modified Gurson-Tvergaard-Needleman (GTN) model, taking into account the structure of the material.

To sum up the results of research it should be noted that:

- application of the modified GTN model taking into account the real parameters of the microstructure of steel S235JR made possible simulation of ductile failure,
- the tensile strength curves obtained by applying global *GTN model* and local *Cell model* were consistent with the experimental results,
- initial process of nucleation and growth of voids was particularly intense in the outer parts of elements; after the maximum force was reached the growth voids rate increased; at the moment when the force decreased suddenly, more intense growth of voids in the middle part in comparison to the outer part of elements was observed,
- the failure growth followed in a very small volume of material, covering the elements lying directly in the plane of the smallest cross section near the bottom of the notch; the same conclusion are drown from both the microstructural studies and numerical simulations,

- application of a local softening of the material (*Cell model*) has significant effects on the evolution of microdamage as compared to the global approach (*GTN model*); the strengthening of the material is observed when the porous material is assumed only in parts of an element (*Cell model*); in such case a sudden drop in load, rapidly leading to the failure of the material is noticed due to the sudden microvoids growth,
- from the point of view of the micro-simulation of the voids evolution, the local approach applied during numerical simulations gives qualitatively better results in comparison to the classical global approach; the assuming of the so-called *process zone*, however, requires determining in advance the places where one would expect nucleation and growth of microvoids, leading eventually to the failure, which in many complex cases can lead to computational errors.

Acknowledgment

The research reported herein was conducted as part of Project R04 007 01 funded over the period 2006–2010 from education budget.

References

1. Bridgman P.W., *Studies in Large Plastic Flow and Fracture*, McGraw-Hill, New York, 1952.
2. Teirlinck D., Zok F., Embury J.D., Ashby M.F., *Fracture Mechanism Maps in Stress Space*, Acta Metallurgica, **36**, 5, 1213–1228, 1988.
3. Gurson A.L., *Continuum Theory of Ductile Rupture by Void Nucleation and Growth: Part I – Yield Criteria and Flow Rules for Porous Ductile Media*, Journal of Engineering Materials and Technology, Transactions of the ASME, **99**, 1, 2–15, 1977.
4. Tvergaard V., *Influence of Voids on Shear Band Instabilities under Plane Strain Conditions*, International Journal of Fracture, **17**, 4, 389–407, 1981.
5. Tvergaard V., Needleman A., *Analysis of the Cup-Cone Fracture in a Round Tensile Bar*, Acta Metallurgica, **32**, 1, 157–169, 1984.
6. PN-EN 1993-1-10:2007 Eurocode 3: Design of Steel Structures – Part 1-10: Material Toughness and Through-thickness Properties.
7. Sedlacek G., Feldmann M., Kühn B., Tschickardt D., Höhler S., Müller C., Hensen W., Stranghöner N., Dahl W., Langenberg P., Münstermann S., Brozetti J., Raoul J., Pope R., Bijlaard F., *Commentary and Worked Examples to EN 1993-1-10 "Material Toughness and Through-Thickness Properties" and Other Toughness Oriented Rules in EN 1993*, JRC Scientific and Technical Reports, European Commission Joint Research Centre, Luxembourg 2008.
8. Tvergaard V., Needleman A., *Effects of Nonlocal Damage in Porous Plastic Solids*, International Journal of Solids and Structures, **32**, 8/9, 1063–1077, 1995.

9. Ramaswamy S., Aravas N., *Finite Element Implementation of Gradient Plasticity Models. Part II: Gradient-dependent Evolution Equations*, Computer Methods in Applied Mechanics and Engineering, **163**, 1–4, 33–53, 1998.

10. Borino G., Failla B., Parrinello F., *A Symmetric Nonlocal Damage Theory*, International Journal of Solids and Structures, **40**, 13–14, 3621–3645, 2003.

11. Kossakowski P., *The simulation of the plastic range for structural steels under multiaxial state of stress basing on the Gurson-Tvergaard-Needleman model* [in Polish: *Symulacja plastycznego zakresu pracy stali konstrukcyjnych w złożonym stanie naprężeń w oparciu o model Gursona-Tvergaarda-Needlemana*], Przegląd Budowlany, **3**, 43–49, 2012.

12. Kossakowski P., *An Analysis of the Load-Carrying Capacity of Elements Subjected to Complex Stress States with a Focus on the Microstructural Failure*, Archives of Civil and Mechanical Engineering, **10**, 2, 15–39, 2010.

13. Kossakowski P.G., Trąmpczyński W., *Numerical simulation of S235JR steel failure with consideration of the influence of microstructural damages* [in Polish: *Numeryczna symulacja zniszczenia stali S235JR z uwzględnieniem wpływu uszkodzeń mikrostrukturalnych*], Przegląd Mechaniczny, **4**, 15–22, 2011.

14. Kossakowski P.G., *Simulation of Ductile Fracture of S235JR Steel Using Computational Cells with Microstructurally-Based Length Scales*, Journal of Theoretical and Applied Mechanics, **50**, 2, 589–607, 2012.

15. Faleskog J., Gao X., Shih C.F., *Cell Model for Nonlinear Fracture Analysis – I. Micromechanics Calibration*, International Journal of Fracture, **89**, 4, 355–373, 1998.

16. Gao X., Faleskog J., Shih C.F., *Cell Model for Nonlinear Fracture Analysis – II. Fracture-Process Calibration and Verification*, International Journal of Fracture, **89**, 4, 375–398, 1998.

17. Corigliano A., Mariani S., Orsatti B., *Identification of Gurson-Tvergaard Material Model Parameters Via Kalman Filtering Technique. I. Theory*, International Journal of Fracture, **104**, 4, 349–373, 2000.

18. Tvergaard V., *Material Failure by Void Growth to Coalescence*, Advances in Applied Mechanics, **27**, 83–151, 1989.

19. The determination of the material structure (taken from the construction), comparative analysis with the parameters of the reference steel [in Polish: *Określenie struktury materiałów (pobranych z konstrukcji), analiza porównawcza z parametrami stali wzorcowej*], Technical report of the Project R04 007 01, Warsaw University of Technology, Warsaw 2008.

20. PN-EN 10002-1:2004 Metallic Materials – Tensile Testing – Part 1: Method of Test at Ambient Temperature.

21. Abaqus 6.10 Analysis User's Manual, Dassault Systèmes, Providence 2010.

22. Richelsen A.B., Tvergaard V., *Dilatant Plasticity or Upper Bound Estimates for Porous Ductile Solids*, Acta Metallurgica et Materialia, **42**, 8, 2561–2577, 1994.

23. Xia L., Shih C.F., *Ductile Crack Growth – I. A Numerical Study Using Computational Cells with Microstructurally-based Length Scales*, Journal of the Mechanics and Physics of Solids, **43**, 2, 233–259, 1995.

24. Xia L., Shih C.F., *Ductile Crack Growth – II. Void Nucleation and Geometry Effects on Macroscopic Fracture Behavior*, Journal of the Mechanics and Physics of Solids, **43**, 12, 1953–1981, 1995.

25. Hancock J.W., Mackenzie A.C., *On the Mechanisms of Ductile Failure in High-strength Steel Subjected to Multi-axial Stress-states*, Journal of Mechanics and Physics of Solids, **24**, 2-3, 147–160, 1976.

Received November 18, 2011; revised version October 1, 2012.